JOURNAL OF PHYSICAL OCEANOGRAPHY

A geometric interpretation of eddy Reynolds stresses in barotropic ocean jets

TALIA TAMARIN*

Department of Earth and Planetary Sciences, Weizmann Institute of Science, Rehovot, Israel.

JAMES R. MADDISON

School of Mathematics and Maxwell Institute for Mathematical Sciences, University of Edinburgh, Edinburgh, United Kingdom

EYAL HEIFETZ

Department of Geophysical Atmospheric and Planetary Sciences, Tel Aviv University, Tel Aviv, Israel

DAVID P. MARSHALL

Department of Physics, University of Oxford, Oxford, United Kingdom

ABSTRACT

Barotropic eddy fluxes are analysed through the geometric properties of the eddy stress tensor. The eddy variance ellipse, describing the mean eddy shape and tilt, is used to elucidate eddy propagation and eddy feedback on the mean flow. Linear shear and jet profiles are analysed and the theoretical results are compared against fully nonlinear simulations. For flows with zero background vorticity gradient, analytic solutions are obtained and provide a direct relationship between the geometric eddy tilt and the phase difference of a normal mode solution. This allows a straightforward interpretation in terms of classical stability theory: the initially unstable jet gives rise to eddies which are tilted against the shear and extract energy from the mean flow. Once the jet stabilizes, eddies become tilted with the shear and return their energy to the mean flow. For a nonzero background vorticity gradient ray-tracing theory is used to investigate eddy propagation within the jet. An analytic solution for the eddy tilt is found for a linear plane Rossby wave on a constant background shear. The ray tracing results broadly agree with the eddy tilt diagnosed from a fully nonlinear simulation.

1. Introduction

The dynamics of the large scale ocean is strongly dependent upon the effect of the small scale turbulent eddy field. The Gent-McWilliams parameterisation (Gent and McWilliams 1990; Gent et al. 1995) is now a key ingredient in coarse resolution ocean circulation models (e.g., Fox Kemper et al. 2013) and can be interpreted as modelling the downward flux of momentum due to eddy form stresses (Greatbatch 1998). This vertical momentum eddy transfer plays a fundamental role in the dynamics of the Southern Ocean (e.g. Johnson and Bryden 1989; Danabasoglu et al. 1994).

While horizontal momentum fluxes are less significant from a global perspective, they can play important roles in the dynamics of inertial jets. For example they influence the dynamics of western boundary currents, where they are instrumental in transferring energy between the mean shear and eddies (Waterman and Jayne 2011; Waterman et al. 2011; Waterman and Jayne 2012). Horizontal eddy stresses are not captured by the Gent and McWilliams parameterisation, and their effect is not typically represented in coarse resolution ocean models (although see e.g. Eden (2010) for an exception). This paper focuses on the study of these horizontal momentum fluxes and their geometric properties.

A number of authors have utilised the Taylor-Bretherton identity (Taylor 1915; Bretherton 1966b; Plumb 1986) to express eddy forcing of the mean flow as the divergence of an eddy stress tensor (Lee and Leach 1996; Cronin 1996; Gent and McWilliams 1996; Young 2012; Marshall et al. 2012; Maddison and Marshall 2013). This formulation leads to a geometric interpretation and, in particular, in the quasi-geostrophic limit leads to a decomposition of the eddy stress in terms of the eddy energy and a number of geometric parameters.

In the barotropic limit this tensor contains the horizontal momentum fluxes, or Reynolds stresses. A norm of this tensor is bounded in terms of the eddy kinetic energy,

*Corresponding author address: Department of Earth and Planetary Sciences, Weizmann Institute of Science, Rehovot 76100, Israel.
E-mail: talia.tamarin@weizmann.ac.il

and this allows its components to be rewritten in terms of the eddy energy and nondimensional parameters describing shape and orientation (Marshall et al. 2012; Waterman and Lilly 2015). This yields a geometric picture, whereby the eddy stress is represented in terms of a variance ellipse (e.g. Morrow et al. 1994; Scott et al. 2008), and is equivalent to a principle component analysis of the anisotropic part of the eddy momentum stresses (Preisendorfer 1988; Waterman and Hoskins 2013).

In Waterman and Hoskins (2013), the geometric properties of the horizontal velocity covariance tensor are used to study the eddy-mean flow interaction in idealized western boundary jet extensions using a barotropic quasi-geostrophic model. An unstable jet is forced at the boundary of the domain and allowed to evolve freely in the interior. The time mean variance ellipses show signatures of jet instability in the upstream unstable region of the jet, and wave radiation in the downstream region. Further, diagnostics of the tilt and anisotropy are shown to be responsible for strengthening and extending the jet in the downstream region, eventually forcing the time-mean recirculation gyres.

The focus of this paper is to study how the geometric interpretation of the eddy fluxes relates to familiar concepts from classical linear stability theory. We study three idealised barotropic configurations: a piecewise linear shear on an f-plane, a piecewise linear jet on an f-plane, and a piecewise linear jet on a β-plane.

For the piecewise linear shear layer on an f-plane, it is shown in the linear case that the eddy tilt is exactly proportional to the normal mode phase difference, yielding a direct interpretation of the eddy tilt in terms of classical stability theory; eddies extract energy from the mean flow when they lean against the shear, consistent with instability, and return energy to the mean flow when they lean with the shear, consistent with stability. The results are additionally interpreted using a Counter-Propagating Rossby Wave perspective (e.g., Bretherton 1966a; Heifetz et al. 1999).

For the piecewise linear jet on an f-plane, an explicit solution is also achieved in the linear case. In addition, we perform a direct numerical simulation which agrees very well with the analytic solution (during the linear stages), and allow a straightforward interpretation in terms of stability arguments. These problems demonstrates the relationship between the eddy variance ellipse, which is conceptually an abstract geometric parameter, and the phase difference between the wave vorticity anomalies.

For the piecewise linear jet on the β-plane, although no analytic solution is presented, these concepts still hold and are used to analyse the dynamics. We diagnose the variance ellipse at different stages of the evolution and show how it corresponds to different characteristics of the zonal mean jet. The eddy tilt and the group velocity (which are intimately related) have in this case a more complex meridional structure, which is a result of the refraction of rays within the jet. Using ray tracing theory, an analytic solution is derived for rays propagating within the layers (far from the interfaces), where only the influence of the β term and a constant shear is felt. The analytic ray tracing solution agrees well with results from a fully nonlinear simulation, with energy radiated into the jet core in the unstable regime and outward in the stable regime.

In each case there is a clear link between the geometric interpretation and the stability of the mean flow. Hence the geometric framework provides an intuitive and unified description of the exchange of energy between the mean flow and the eddies, the direction of eddy propagation, and the orientation of the eddies with respect to the mean shear.

The paper is organized as follows. In Section 2 we review the basic ingredients of eddy-mean flow interaction from a geometric perspective. In Section 3 we employ the geometric decomposition for simple barotropic flows. We present analytic results for a piecewise linear shear layer and piecewise linear jet on an f-plane. For the latter, results are also compared to a direct numerical simulation. A numerical simulation for the case of a barotropic piecewise linear jet on a β plane is presented and the geometric perspective is used to analyse the dynamics. We discuss the relationship between these results and those described in Waterman and Hoskins (2013) for a zonally evolving jet. In Section 4 ray tracing theory is reviewed and used to develop an analytic solution for the piecewise linear jet on a β-plane. The theoretical predictions are compared against the results from a fully non-linear simulation. In section 5 the key results are summarised, with a discussion as to how the ideas developed in this article may be exploited to parameterise eddy Reynolds stresses in numerical ocean circulation models.

2. Geometric framework

a. Theoretical background

The mean barotropic vorticity equation, neglecting forcing and dissipation, can be written as

$$\frac{\partial \bar{q}}{\partial t} + \bar{\mathbf{u}} \cdot \nabla \bar{q} = -\nabla \cdot (\overline{\mathbf{u}'q'}) \tag{1}$$

where the bar signifies an appropriate averaging operator and the prime is a deviation from that average[1],

$$q = f + \frac{\partial v}{\partial x} - \frac{\partial u}{\partial y} \tag{2}$$

is the absolute vorticity, f is the planetary vorticity and $\mathbf{u}$ is the non-divergent velocity. The eddy vorticity forcing,

$$\nabla \cdot (\overline{\mathbf{u}'q'}) = \left(\frac{\partial^2}{\partial x^2} - \frac{\partial^2}{\partial y^2} \right) \overline{u'v'} + \frac{\partial^2}{\partial x \partial y} \left(\overline{v'^2} - \overline{u'^2} \right), \tag{3}$$

[1]The averaging operator is linear, commutes with the partial derivatives $\partial/\partial x$, $\partial/\partial y$, $\partial/\partial t$ and satisfies a Cauchy-Schwartz inequality such that $\overline{a'b'}^2 \leq \overline{a'^2}\,\overline{b'^2}$, with $\overline{a'^2} \geq 0$.

originates from the double divergence of the *eddy flux tensor*,

$$\mathbf{T} = \begin{pmatrix} N & M-K \\ M+K & -N \end{pmatrix}, \tag{4}$$

where

$$M = \frac{1}{2}\left(\overline{v'^2} - \overline{u'^2}\right), \quad N = \overline{u'v'} \tag{5}$$

represent the eddy momentum fluxes or *Reynolds stresses* and

$$K = \frac{1}{2}\left(\overline{u'^2} + \overline{v'^2}\right) \tag{6}$$

is the eddy kinetic energy.

As described in Maddison and Marshall (2013), since the double divergence of the eddy flux tensor is the eddy vorticity tendency, the divergence of the eddy flux tensor is equal to the eddy vorticity flux plus a rotational term, i.e., there are two sources of gauge freedom. In particular, the vorticity equation is unaffected by the addition of any antisymmetric tensor to the eddy flux tensor. Hence, for this simple case, we can eliminate the eddy kinetic energy term, which contributes only rotational flux, and choose

$$\mathbf{T}^* = \begin{pmatrix} N & M \\ M & -N \end{pmatrix}. \tag{7}$$

The eddy flux tensor is closely related to the *eddy stress tensor* whose divergence appears as the eddy forcing on the right-hand side of the residual-mean momentum equation (e.g., Hoskins et al. 1983; Plumb 1986; Cronin 1996; see Maddison and Marshall 2013 for further details).

Hoskins further consider the gauge

$$\mathbf{T_H}^* = \begin{pmatrix} N & 2M \\ 0 & -N \end{pmatrix} \tag{8}$$

and thus, by considering the limit where $N_{xx} \approx 0$, define the *E-vector*, $\mathbf{E}_H = (2M, -N)^T$, that captures the dynamically significant components of the eddy flux tensor.[2] This has proven very useful in studying the eddy-mean flow interaction, especially in the atmospheric context. In general, different gauge choices lead to different eddy stress tensors and corresponding residual mean velocities (see Maddison and Marshall 2013 for a detailed discussion), but the overall dynamics is unaffected by the choice of gauge.

b. Geometric decomposition

Following Hoskins et al. (1983) and Waterman and Hoskins (2013), the eddy flux tensor (7) can provide information on the average eddy shape, orientation, propagation and mean flow feedback. In the rest of the section we will review some of the fundamental ideas behind the geometric decomposition and its relation to the eddy-mean flow interaction.

[2]Strictly $\mathbf{E}_H$ is a quasi-vector since it does not transform as a vector (Hoskins et al. 1983)

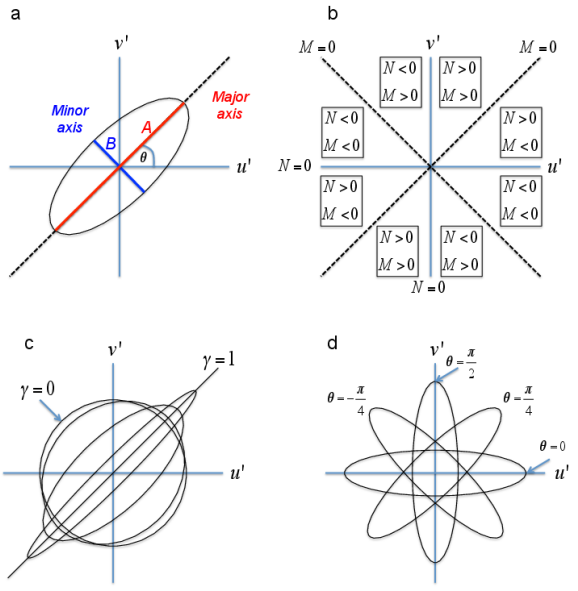

FIG. 1. (a) Eddy variance in the (u', v') space is represented by an ellipse with a major and minor axes (the red and blue lines denoted as A and B, respectively) (see also Marshall et al. (2012) figure 3 (a)). (b) Depending on the signs of the Reynolds stresses M and N, the diagram shows the corresponding location of the major axis (with a π rotation symmetry). The $\hat{x}$ and $\hat{y}$ axes correspond to solutions with $N = 0$, for which the eddy ellipse is either zonally or meridionaly elongated, while the dashed lines correspond to solutions with $M = 0$ (see also Waterman and Hoskins (2013) figure 2). (c) Schematic illustration of possible eddy ellipse anisotropy, from $\gamma = 0$ which is a perfect circle to $\gamma = 1$ which is a line. (d) Schematic illustration of possible eddy ellipse tilt. For $\theta = \pi/2$ the eddy ellipse is stretched along the meridional direction, while for $\theta = 0$ it is along the zonal direction. For $0 < \theta < \pi/2$ ("positive tilt") the major axis is within the first quadrant, and for $-\pi/2 < \theta < 0$ ("negative tilt") it is in the fourth quadrant.

Since the Reynolds stresses satisfy $M^2 + N^2 \leq K^2$, a norm of the eddy stress tensor is bounded in terms of the eddy kinetic energy. Hence, one may write, without loss of generality,

$$M = -\gamma K \cos 2\theta, \quad N = \gamma K \sin 2\theta \tag{9}$$

where $0 \leq \gamma \leq 1$ is an anisotropy parameter, determined by the ratio of the Reynolds stresses to the eddy kinetic energy,

$$\gamma = \frac{\sqrt{M^2 + N^2}}{K}, \tag{10}$$

and the orientation of the averaged eddy momentum fluxes satisfies

$$\tan 2\theta = -\frac{N}{M}, \tag{11}$$

where we define $-\pi/2 \leq \theta \leq \pi/2$.

The correct quadrant of θ depends on the signs of M and N (see Fig. 1b). These parameters are exactly the velocity variance ellipse eccentricity and tilt, described in

Preisendorfer (1988), which characterize an ellipse whose major and minor axes explain the velocity covariance. Fig. 1a shows a schematic illustration of the variance ellipse and its characteristics.

The eddy velocity correlation can plotted in the (u',v') space, where each point is measured at a different time during the evolution of the flow (or at a different spatial location). The time (or spatially) averaged "eddy" can then be represented by an ellipse, as in Fig. 1a, with a semi-major A and semi-minor B axes (the red and blue lines, respectively), given by

$$A=\sqrt{2(1+\gamma)K};\quad B=\sqrt{2(1-\gamma)K} \tag{12}$$

Note that this ellipse does not, in general, have a direct relation to the eddy structure in the physical (x',y') space.

The tilt θ of the ellipse describes the locally dominant direction of the eddy momentum fluxes. The eccentricity or *anisotropy* parameter γ describes how preferentially the momentum fluxes are directed in this dominant direction. Values of anisotropy close to unity (high anisotropy) imply that the eddy momentum fluxes are strongly oriented in the direction of the ellipse tilt. If $\gamma=1$, for which the ellipse is a straight line, then the momentum flux in the direction orthogonal to the tilt is zero. Conversely if $\gamma=0$, for which the ellipse is a circle, momentum fluxes are isotropically distributed in all directions and there is no locally dominant eddy momentum flux direction. A general mapping of the major axis tilt, for different signs of the Reynolds stresses M and N, is shown in Fig. 1b. The diagram shows the corresponding octant of the major axis, which is symmetric under $\pm\pi$ rotations. Fig. 1c shows some possible eddy ellipse anisotropies, and Fig. 1d is a schematic illustration of possible eddy ellipse tilts.

c. Relation to propagation of eddy activity

A further interesting relation exists, in certain cases, between the direction of the relative group velocity[3] of eddy activity, and the eddy variance ellipse (Plumb 1986; Hoskins et al. 1983; Maddison and Marshall 2013; Waterman and Hoskins 2013). The relation between the tilt and group propagation, described in Hoskins et al. (1983) and Waterman and Hoskins (2013), are key to the ray tracing analysis of Section 4. Specifically, it follows that for a two dimensional plane wave with streamfunction[4]

$$\psi'=\hat{\psi}e^{i(kx+ly-\omega t)}, \tag{13}$$

we have $\gamma=1$ and the eddy ellipse tilt is given by

$$\tan 2\theta=\frac{2kl}{k^2-l^2}. \tag{14}$$

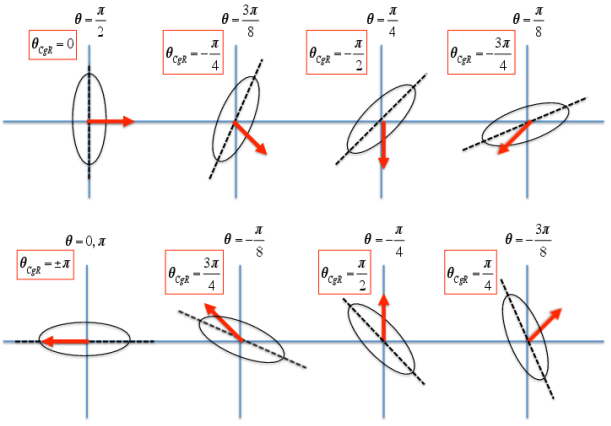

FIG. 2. The relation between the eddy ellipse axis and direction of the relative group velocity (after Fig. 4 of Hoskins et al. 1983). Plotted are different eddy ellipse tilts and the corresponding direction of the relative group velocity $\mathbf{c}_{gR}=\mathbf{c}_g-\bar{\mathbf{u}}$ (red arrows) for $\bar{q}=\beta y$ (with $\beta>0$). The dashed black line shows the major axis of the eddy ellipse, and the red arrow is the relative group velocity. The first row is characterized by $N\geq 0$ and $c_{g_{Ry}}\leq 0$ while for the second row $N\leq 0$ and $c_{g_{Ry}}\geq 0$.

Since velocity anomalies are aligned with the direction of phase propagation for a plane wave, the eddy ellipse tilt also satisfies

$$\tan\theta=\frac{l}{k}. \tag{15}$$

It is straightforward to show that (14) and (15) are equivalent through a standard trigonometric identity.

Furthermore, assuming the barotropic Rossby wave dispersion relation on a β-plane,

$$\omega=\bar{u}k-\frac{\beta k}{k^2+l^2}, \tag{16}$$

where the mean flow is zonal and constant, or slowly varying, $\bar{\mathbf{u}}=(\bar{u},0)$. If follows from direct substitution of

$$c_{gx}=\frac{\partial\omega}{\partial k}=\bar{u}+\frac{\beta(k^2-l^2)}{(k^2+l^2)^2},\quad c_{gy}=\frac{\partial\omega}{\partial l}=\frac{2\beta kl}{(k^2+l^2)^2} \tag{17}$$

that

$$\mathbf{c}_{gR}=\mathbf{c}_g-\bar{\mathbf{u}}=\frac{\beta}{\frac{1}{2}\overline{q'^2}}(M,-N). \tag{18}$$

Hence, if θ_{CgR} is the angle of the relative group velocity (the subscript $_R$ indicating "relative to the mean flow"), we find that

$$\tan\theta_{C_{gR}}=\frac{c_{gy}}{c_{gx}-\bar{u}}=-\frac{N}{M}=\frac{2kl}{k^2-l^2}. \tag{19}$$

Thus

$$\theta_{CgR}=2\theta\mp\pi, \tag{20}$$

where the minus sign corresponds to $N>0$ and the positive sign corresponds to $N<0$, chosen such that $-\pi\leq$

[3] Here the "relative" group velocity refers to the group velocity relative to the mean. Thus is also known as the "intrinsic" group velocity (e.g., Buhler 2009).

[4] Hereafter it is understood that the real part of complex functions is to be taken where relevant.

$\theta_{CgR} \leq \pi$. The need for the phase shift is clear from considering the signs of M and N in (18). These relationships are summarised in Fig. 2. The first row corresponds to situations in which $N \geq 0$ and the eddy ellipse tilt is positive giving $c_{g_{R_y}} \leq 0$; conversely the second row corresponds to situations in which $N \leq 0$ and the eddy ellipse tilt is negative giving $c_{g_{R_y}} \geq 0$.

Note that in the more general case,

$$\mathbf{c}_{gR} = \frac{1}{\frac{1}{2}\overline{q'^2}} \left(M\frac{\partial \bar{q}}{\partial y} + N\frac{\partial \bar{q}}{\partial x}, M\frac{\partial \bar{q}}{\partial x} - N\frac{\partial \bar{q}}{\partial y} \right), \qquad (21)$$

i.e., the relation (18) still holds but in a coordinate system rotated along and across the mean absolute vorticity gradient (Hoskins et al. 1983; Waterman and Hoskins 2013).

3. Geometric decomposition for piecewise linear flows

In order to study the geometric properties of the eddy fluxes, we consider simple configurations consisting of a barotropic piecewise linear shear layer and a piecewise linear jet. For the cases where only shear instability is considered (i.e., on an f plane), analytic solutions are found for the linear normal modes, and the geometric decomposition of the eddy stress tensor is calculated directly. Numerical simulations of the barotropic jet are performed on both f and β planes and these are compared against the normal mode solutions. The eddy-mean flow interaction is examined via diagnostics of the geometric properties of the eddy stress tensor. For the case of a barotropic jet on a β plane, ray tracing theory is used to explain the meridional structure of the eddy ellipse, and in particular how this is related to the propagation of eddy activity.

a. Piecewise linear shear layer on an f-plane

For a single shear layer with negative vorticity embedded by two infinite layers of zero vorticity (the Rayleigh model, see Fig. 3a), we find that the eddy tilt is directly related to the normal mode phase difference. This allows a direct interpretation of the eddy tilt in terms of the linear wave instability results.

Consider the Rayleigh model basic state sketched schematically in Fig. 3a, that supports the existence of counter propagating Rossby wave pairs on the two sides of the shear layer, whose zonal mean velocity and vorticity are given by:

$$\bar{u}(y) = \begin{cases} \Lambda b & y \geq b \\ \Lambda y & -b \leq y \leq b \\ -\Lambda b & y \leq -b \end{cases}, \qquad (22)$$

$$\bar{q}(y) = \begin{cases} 0 & y > b \\ -\Lambda & -b < y < b \\ 0 & y < -b \end{cases}. \qquad (23)$$

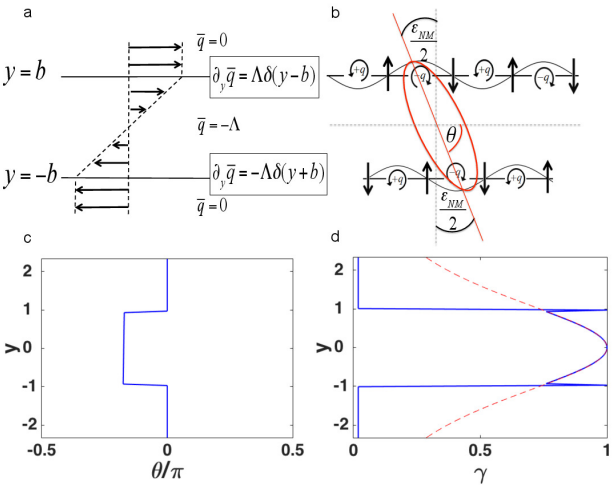

FIG. 3. (a) The Rayleigh model (left), a piecewise linear velocity profile of a single shear layer with negative vorticity embedded by two infinite layers of zero vorticity. At $y = \pm b$ the mean flow vorticity is discontinuous, yielding a positive/negative mean vorticity gradient delta function there, respectively. (b) Schematic illustration of the most unstable normal mode configuration, which is composed of two phased locked counter propagating Rossby waves ($\varepsilon_{k_{max}} \cong 0.65\pi$), and the corresponding eddy ellipse (red ellipse), which is tilted against the shear. The ellipse tilt θ is related to the normal mode phase difference by $\theta = \varepsilon_{NM}/2 + \pi/2$. The $\pm q$ symbols denote positive/negative vorticity anomalies, and the arrows show the circulation they induce. (c) The eddy ellipse tilt $\theta \approx -0.17\pi$ given by the normal mode solution, which is constant within the shear layer.(d) The eddy ellipse anisotropy. For reference, $\cosh^{-1}(2ky)$ is shown in light red. At $y = \pm 1$ and at the center of the shear layer $\gamma = 1$ (here $y = y/b$ is the nondimensional meridional coordinate).

Let the bar and prime now indicate zonal mean and perturbation respectively. For horizontally nondivergent eddies, we have

$$\overline{u'q'} = \frac{\partial M}{\partial y}, \quad \overline{v'q'} = -\frac{\partial N}{\partial y}, \qquad (24)$$

Hence, in those regions where $q' = 0$, both M and N are independent of y. We therefore need to determine single values for M and N in each of the three regions: $y < -b$, $-b < y < b$ and $y > b$.

The normal mode solution for a small disturbance are obtained from the linearized vorticity equation,

$$\left[\frac{\partial}{\partial t} + \bar{u}\frac{\partial}{\partial x}\right] q' = -v'\frac{\partial \bar{q}}{\partial y}, \qquad (25)$$

Since $\partial\bar{q}/\partial y$ is concentrated in two δ-functions at $y = \pm b$, the vorticity perturbation is also concentrated there as δ-functions. For a given wavenumber k we can write

$$q'_k = Q_k \left[e^{i\varepsilon_k^b}\delta(y-b) + e^{i\varepsilon_k^{-b}}\delta(y+b) \right] e^{ikx}, \qquad (26)$$

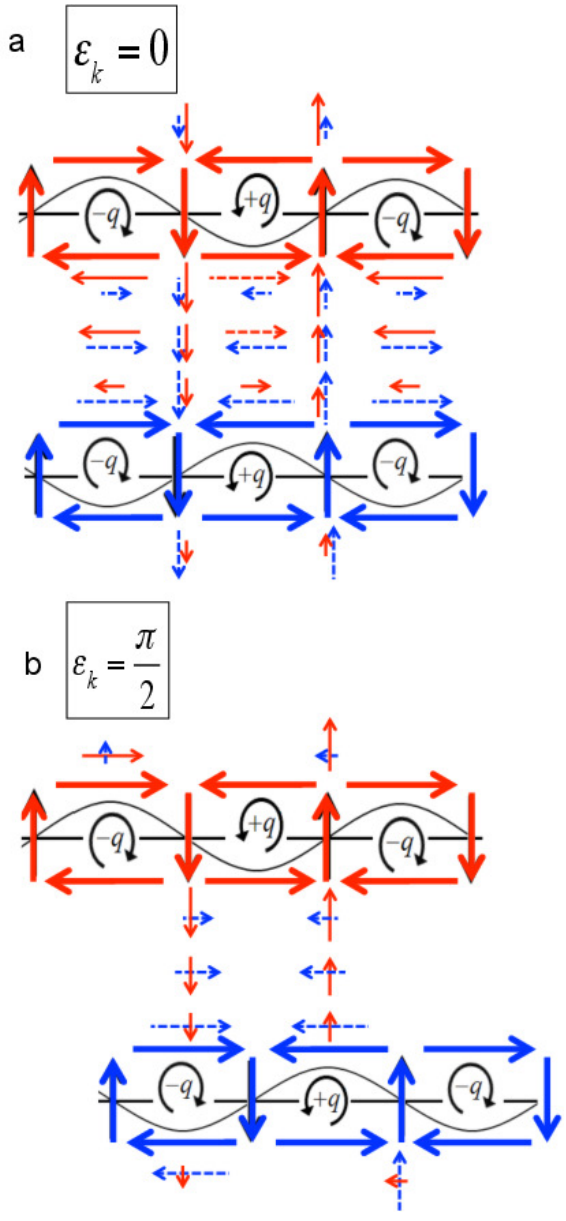

FIG. 4. Schematic illustration of two isolated vorticity waves and their induced velocities, when the waves are (a) in phase ($\varepsilon_k = 0$), and (b) $\pi/2$ out of phase ($\varepsilon_k = \pi/2$). The $\pm q$ and circular arrows show the vorticity anomaly, the black thick arrows represent their associated velocities. The red and dashed blue arrows represent the induced velocities from the upper and lower waves, respectively. The figure illustrates how M (N) is maximized when the waves are in phase ($\pi/2$ out of phase)

.

where $Q_k(t)$ is the amplitude of the vorticity perturbations (equal by symmetry), and $\varepsilon_k^b(t)$, $\varepsilon_k^{-b}(t)$ are the phases of the waves at $y = b, -b$ respectively. We can find the corresponding streamfunction using the appropriate Green's function,

$$\psi_k' = -\frac{Q_k}{2k}\left[e^{i\varepsilon_k^b}e^{-k|y-b|} + e^{i\varepsilon_k^{-b}}e^{-k|y+b|}\right]e^{ikx}. \tag{27}$$

The resultant velocity anomalies in the first and third regions are

$$\begin{aligned} &y < -b: \\ &u_k' = iv_k' = \frac{Q_k}{2}\left[e^{i\varepsilon_k^b}e^{k(y-b)} + e^{i\varepsilon_k^{-b}}e^{k(y+b)}\right]e^{ikx}, \\ &y > b: \\ &u_k' = -iv_k' = -\frac{Q_k}{2}\left[e^{i\varepsilon_k^b}e^{-k(y-b)} + e^{i\varepsilon_k^{-b}}e^{-k(y+b)}\right]e^{ikx}. \end{aligned} \tag{28}$$

Substituting the above into (5) it follows that

$$M,\ N = 0 \quad \text{for } y < -b \text{ and } y > b. \tag{29}$$

However, if $-b < y < b$, then:

$$u_k' = \frac{Q_k}{2}\left[e^{i\varepsilon_k^b}e^{k(y-b)} - e^{i\varepsilon_k^{-b}}e^{-k(y+b)}\right]e^{ikx}, \tag{30}$$

$$v_k' = -\frac{Q_k}{2}i\left[e^{i\varepsilon_k^b}e^{k(y-b)} + e^{i\varepsilon_k^{-b}}e^{-k(y+b)}\right]e^{ikx}, \tag{31}$$

giving

$$M = \frac{Q_k^2}{4}e^{-2kb}\cos\varepsilon_k, \quad N = -\frac{Q_k^2}{4}e^{-2kb}\sin\varepsilon_k, \tag{32}$$

where $\varepsilon_k = \varepsilon_k^b - \varepsilon_k^{-b}$ is the phase difference between the waves and is independent of time. Noting the corresponding expression for the eddy kinetic energy,

$$K = \frac{Q_k^2}{4}e^{-2kb}\cosh(2ky), \tag{33}$$

the eddy tilt and anisotropy are given by

$$\theta = \frac{\varepsilon_k}{2} \pm \frac{\pi}{2}, \quad \gamma = \operatorname{sech}(2ky), \tag{34}$$

with the sign of the phase shift chosen to ensure $-\pi/2 \leq \theta \leq \pi/2$.

In summary, the Reynolds stresses vanish outside the shear layer and have constant values within the shear layer, the latter depending on the phase difference between the two interacting vorticity waves; this result is generalized in Appendix A for a continuous vorticity profile and shown to hold between any two vorticity waves. A corollary is that the eddy tilt, but not the eddy anisotropy, is constant within the shear layer.

Fig. 4 shows schematically the velocity field induced by the pair of vorticity waves for the two cases where they are (a) in phase ($\varepsilon_k = 0$) and (b) $\pi/2$ out of phase ($\varepsilon_k = +\pi/2$), illustrating that the magnitude of M is greatest and

N vanishes when the waves are in phase; conversely the magnitude of N is greatest and M vanishes when the waves are $\pi/2$ out of phase.

Equation (34) provides a direct link between the geometric interpretation of the eddy Roynolds stresses and classical stability theory. The normal mode growth rate from linear instability for a counter propagating Rossby wave pair is given by the expression $(\Lambda/2)e^{-2kb}\sin\varepsilon_k$ (Heifetz et al. 1999). Thus for a given shear Λ and wavenumber k, the growth rate depends entirely on the phase difference between the waves. Growing solutions are achieved for $0<\varepsilon_k<\pi$, when the waves are mutually amplifying each other. The maximum instantaneous growth is achieved when the phase difference is exactly $\pi/2$. Stable solutions are modes for which $-\pi<\varepsilon_k<0$, where the waves are mutually destroying each other. Hence, via (34), the eddy ellipse of an unstable solution, that extracts energy from the mean flow, leans *against* the shear ($-\pi/2<\theta<0$), and the eddy ellipse of a stable normal mode solution, which returns energy to the mean flow, leans *with* the shear ($0<\theta<\pi/2$), as discussed by Marshall et al. (2012).

Fig. 3b shows a schematic illustration of the most unstable normal mode configuration which is composed of two phased locked counter propagating Rossby waves at $y=\pm b$, and the corresponding eddy ellipse which is tilted against the shear. Linear stability analysis reveals that the asymptotically most unstable mode has normalized wavenumber $2k_{max}b\cong 0.8$ with phase difference of $\varepsilon_{k_{max}}\cong 0.65\pi$ (Heifetz et al. 1999), which gives $\theta\cong -0.17\pi$. The results for this problem are shown if Fig. 3c, d, where we use the theoretical streamfunction, given by Eq. (38) for the most unstable mode, to calculate the tilt and anisotropy. Fig. 3c shows that the eddy ellipse is characterized by a negative constant tilt within the shear layer, which implies that the eddy is indeed tilted against the shear. Fig. 3d shows that anisotropy is discontinuous at the interfaces where the δ-function waves exist. It goes from zero outside the shear layer to exactly one on the interfaces, and to a value of $\mathrm{sech}(2k_{max}b)\cong\mathrm{sech}(0.8)\cong 0.74$ close to the interfaces from the inner side. For reference, a plot of $\mathrm{sech}(2ky)$ is also shown in Fig. 3d (red thin line). Inside the shear layer, anisotropy increases to unity towards the center of the shear layer. This means that inside the layer, momentum fluxes are quite anisotropic so the eddy variance ellipse is elongated along a direction that has a specific orientation (in this case, such that the momentum fluxes are negative and tend to decrease the shear). The expressions for γ and θ are independent of the amplitude of the normal mode solution and depend only on the wavenumber k, since by construction a normal mode solution satisfies $\cos\varepsilon_k=e^{-2kb}(2kb-1)$, achieved by the phase locking requirement (Heifetz et al. 1999; Pedlosky 1979).

b. Piecewise linear jet on an f-plane

Following a similar procedure as for the piecewise linear shear layer, one can find the analytic linear normal mode solutions for a piecewise linear jet, which consists of two vorticity strips (e.g., Heifetz et al. 1999). While highly idealized, this piecewise linear model may provide qualitatively useful information about the linear wave development and the essence of the instability process in more realistic oceanic jets.

The basic state (Fig. 5a) is given by

$$\bar{u}(y)=\begin{cases}0 & y\geq b\\ \Lambda(b-y) & 0\leq y\leq b\\ \Lambda(b+y) & -b\leq y\leq 0\\ 0 & y\leq -b\end{cases}, \tag{35}$$

$$\bar{q}(y)=\begin{cases}0 & y>b\\ \Lambda & 0<y<b\\ -\Lambda & -b<y<0\\ 0 & y<-b\end{cases}. \tag{36}$$

In this case, the solution consists of three waves, at each of the interfaces $y=0,\pm b$, and the vorticity field for a given wavenumber k can be written as

$$\begin{aligned}q'_k=&[Q_k^b e^{i\varepsilon_k^b}\delta(y-b)+Q_k^0 e^{i\varepsilon_k^0}\delta(y)\\ &+Q_k^{-b}e^{i\varepsilon_k^{-b}}\delta(y+b)]e^{ikx}.\end{aligned} \tag{37}$$

For a symmetric normal mode solution we have $Q_k(t)=Q_k^b=Q_k^{-b}=Q_k^0/2$, $\varepsilon_k^b=\varepsilon_k^{-b}$, and we define the phase difference $\varepsilon_k\equiv\varepsilon_k^0-\varepsilon_k^b=\varepsilon_k^0-\varepsilon_k^{-b}$ which is is independent of time.

The corresponding streamfunction, which can be found using the appropriate Green's function, is then

$$\psi'_k=-\frac{Q_k}{2k}\left[e^{-k|y-b|}+2e^{i\varepsilon_k}e^{-k|y|}+e^{-k|y+b|}\right]e^{ikx}. \tag{38}$$

On each side of the jet, we find that the Reynolds stresses are again independent of y,

$$M=\frac{Q_k^2}{2}e^{-kb}\left(\cos\varepsilon_k+\frac{e^{-kb}}{2}\right),\quad N=\pm\frac{Q_k^2}{2}e^{-kb}\sin\varepsilon_k, \tag{39}$$

and the geometric properties of the eddy ellipse are given by

$$\tan 2\theta=\mp\frac{\sin\varepsilon_k}{\cos\varepsilon_k+\frac{1}{2}e^{-kb}}; \tag{40}$$

$$\gamma=\frac{\sqrt{1+\frac{1}{4}e^{-2kb}+e^{-kb}\cos\varepsilon_k}}{\frac{1}{2}e^{-kb}\cosh(2ky)+e^{-2ky}(\cos\varepsilon_k+e^{kb})}, \tag{41}$$

where the negative sign in (40) corresponds to the cyclonic side of the jet ($0<y<b$) and the positive sign to the anticyclonic side of the jet ($-b<y<0$). The eddy ellipse

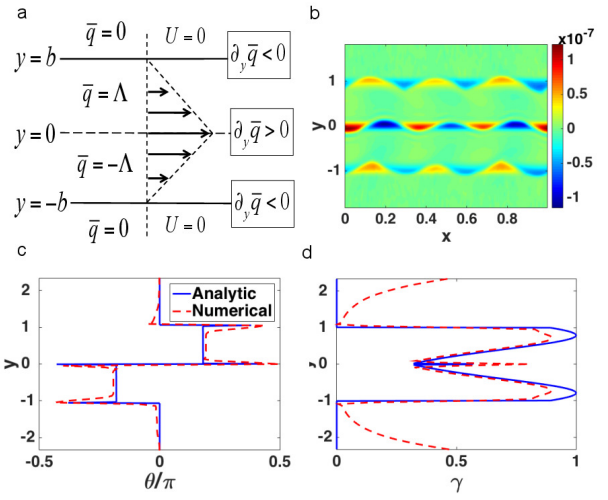

FIG. 5. (a) The piecewise linear jet model of two shear layer with constant vorticity of opposite signs embedded by two infinite layers of zero vorticity. At $y = 0, \pm b$ the mean flow vorticity is discontinuous, and supports the existence of three waves on each of the interfaces. (b) Snapshot of relative vorticity (s^{-1}) at some initial time evolution, after $t = 25$ days, shows the most unstable normal mode configuration of three phase locked waves which are tilted against the shear. (c) The eddy ellipse tilt given by the normal mode solution (blue line) is constant within each side of the jet, and equals $\theta \cong \pm 0.18\pi$, This is in good agreement with the snapshot from a numerical simulation (red dashed line) at day $t = 25$. (d) The eddy ellipse anisotropy from the analytic solution (blue) and the numerical simulation (dashed red). At each of the interfaces $y = 0, \pm 1$ (here $y = y/b$ is the nondimensional meridional coordinate) the anisotropy maximizes.

.

tilt is no longer directly proportional to the normal mode phase difference due to the interaction with the third vorticity wave, which gives an additional $\frac{1}{2}e^{-kb}$ term in the denominator of (40). However, the normal mode phase difference ε_k is still a known function of k, found using the normal mode phase locking requirement.

From linear stability analysis, one can find that the asymptotically most unstable normal mode for the piecewise linear jet (Heifetz et al. 1999) has a normalized wavenumber $2k_{max}b \cong 2.452$ and phase difference $\varepsilon_{k_{max}} \cong 0.68\pi$, which gives an eddy ellipse tilt of $\theta \cong 0.18\pi$ in the cyclonic side of the jet and $\theta \cong -0.18\pi$ in the anticyclonic side of the jet. Hence, the eddy ellipse is tilted *against* the shear in each side of the jet, consistent with the unstable normal mode solution, fluxing momentum out of the jet core and into its flanks thus overall acting to decrease the shear.

The results for this problem are shown if Fig. 5 where we compare the theoretical prediction for the eddy ellipse tilt and anisotropy to a fully nonlinear simulation. Details regarding the numerical model are given in Appendix B. The non-differentiable piecewise-linear jet in (35) is approximated by a smooth "tanh" profile whose vorticity is given by

$$q_0 = \frac{\Lambda}{2}\left[2\tanh\left(\frac{y}{d}\right) - \tanh\left(\frac{y+b}{d}\right) - \tanh\left(\frac{y-b}{d}\right)\right] \tag{42}$$

where Λ is the shear, the interfaces of the layers are located at $y = 0, \pm b$ ($b \cong 430km$), and δ is a parameter that measures the relative thickness of the transition regions at the interfaces. In the limit $d \to 0$, one recovers the piecewise linear profile. Here a small value of $d = 0.05\,b$ is chosen. The zonal mean flow, absolute vorticity and absolute vorticity gradient of the approximated piecewise linear jet are shown in Fig. 6, where the black solid line indicates the initial conditions at day $t = 0$.

A snapshot of the relative vorticity at early stages of the simulation, after $t = 25$ days (Fig. 5b), shows that the vorticity perturbation is localized at the three interfaces $y = 0, \pm b$. The system picks up the most unstable normal mode solution, which is tilted against the shear in each layer. Fig. 5c, d shows the zonally averaged eddy ellipse tilt and anisotropy, respectively, from the numerical simulation (dashed red line) and the analytic solution (blue line), calculated using the streamfunction expression for the most unstable normal mode. The results are in very good agreement, and show that the eddy tilt is constant and positive (negative) in the cyclonic (anticyclonic) side of the jet, with a jump towards $\pm\pi/2$ at $y = 0$. The anisotropy structure in each of the layers is similar to that for the single shear layer case, though here it maximizes closer to the edges $y = \pm b$ rather than in the middle of the layer. Both M and N are constant within the layers, and hence only the perturbation kinetic energy K controls the meridional structure of the anisotropy γ (which is inversely proportional to K).

The constant tilts remain close to the theoretical value even at later stages of the simulation, when the waves merge into vortices (not shown). At much later stages of the development, however, the linear solution does not describe the dynamics adequately. In addition, once the mean vorticity gradient becomes nonzero, the tilt is no longer constant. This is examined in more detail in the next section in which we add a background planetary vorticity gradient. Since there are many similarities between the results obtained on the f plane and β plane, we defer a more detailed discussion until the latter case.

c. Piecewise linear jet on a β-plane

A more physically relevant case is when a background planetary vorticity gradient is included. The analytic solution derived in the previous section is no longer valid since the eddy ellipse tilt is no longer constant. Nonetheless, the tilt derived for the f plane (40) gives a good estimate of the tilt close to the jet flanks at $y = \pm b$ (though it increases monotonically towards the jet core, for example as in Fig.

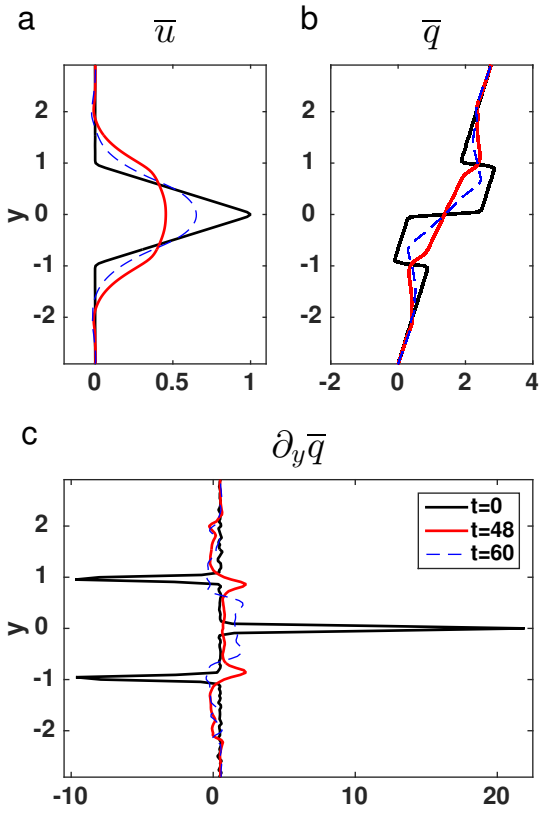

FIG. 6. (a) Zonal mean velocity (normalized by $U_{0max} = 0.04\,\mathrm{m\,s^{-1}}$) at three different times of the evolution. The initial piecewise linear jet (day $t = 0$, black solid line) weakens and broadens significantly due to eddies fluxing momentum out of the jet (day $t = 48$, red), but later strengthens due to upgradient fluxes (day $t = 60$, dashed blue). (b) Zonal mean potential vorticity (normalized by $\Lambda = 9.3 \times 10^{-8}\,\mathrm{s^{-1}}$) and (c) mean potential vorticity gradient (normalized by $b^{-1}\Lambda = 2.16 \times 10^{-13}\,\mathrm{m^{-1}s^{-1}}$), for three different times of the evolution. At day $t = 0$ the potential vorticity has sharp opposite steps, and the potential vorticity gradient changes sign. At day $t = 48, 60$ the potential vorticity gradient no longer changes sign within the domain. Here $y = y/b$ is the nondimensional meridional coordinate.

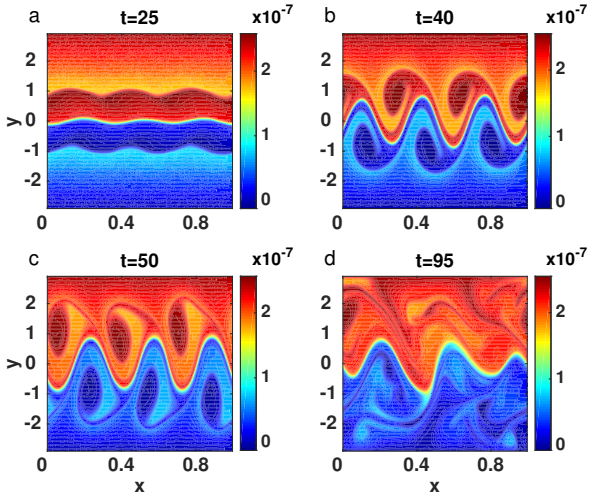

FIG. 7. Snapshots of the potential vorticity ($\mathrm{s^{-1}}$) at different times of the evolution (time units is given in days). (a) day $t = 25$, the most unstable mode is apparent and the interfaces are characterized by a wavy structure. (b) day $t = 40$, the system is no longer in the linear stage as the waves merged into vortices, however they are still clearly tilted against the shear. (c) day $t = 50$, the tilt flips and the vortices are now tilted with the shear. (d) day $t = 95$, the vortices break and only one clear undulating interface exist. Here $y = y/b$ is the nondimensional meridional coordinate.

12). In order to capture the meridional dependence of the tilt, we will study it in detail using ray tracing theory as discussed in section 4, but first we give a simple qualitative description of the evolution of the flow.

Fig. 7 shows snapshots of the potential vorticity field at different stages of the simulation, where time is normalized to days. Initially (day $t = 25$) the system behaves linearly, the interfaces are characterized by a wavy structure and the perturbation relative vorticity (not shown) is characterized by three waves at each of the interfaces, with a wavenumber corresponding to that of the most unstable mode. At later times (day $t = 40$), the solution is dominated by vortices (rather then waves), which appear to be tilted against the shear. The orientation of the vortices changes shortly afterwards (day $t = 50$), and become tilted with the shear. Eventually (day $t = 95$), the vortices break nonlinearly and the system equilibrates with one undulating interface.

The zonal mean velocity, absolute vorticity and absolute vorticity gradient are plotted in Fig. 6 for three different times of the simulation. The initial flow (day $t = 0$, black solid line) is identical to that used in the non-zero beta case, i.e. the smooth approximation of the piecewise linear jet. Fig. 6a shows the non dimensional zonal speed (normalized by the maximum velocity in the initial jet), Fig. 6b shows the corresponding nondimensional mean potential vorticity and Fig. 6c the mean potential vorticity gradient (normalized by Λ^{-1} and $b\Lambda^{-1}$, respectively). As can be seen, the initial mean flow is indeed barotropically unstable: it satisfies necessary conditions for instability in that the absolute vorticity gradient $\partial\bar{q}/\partial y$ changes sign within the domain and is positively correlated with the mean flow.

By day $t = 48$, the mean flow has become much weaker due to the transfer of energy from the mean flow to the eddies (not shown). At this instant, the behaviour of the system changes dramatically: $\partial\bar{q}/\partial y$ ceases to change sign within the domain (red solid line in Fig. 6b) and so the jet can no longer support the existence of linearly unstable solutions. At later times (day $t = 60$, dashed blue line), *jet sharpening* can be identified in which the mean flow has strengthened as a result of up-gradient eddy momentum fluxes into the core of the jet.

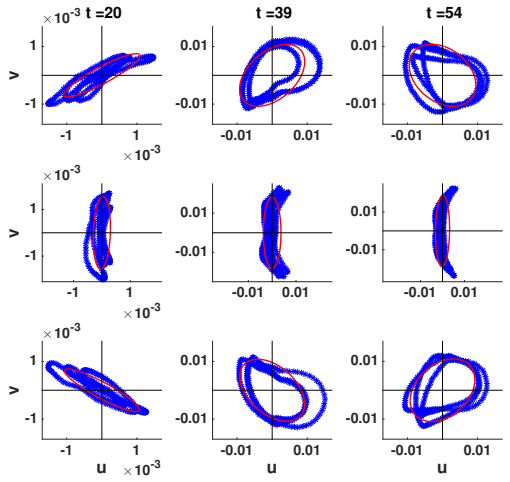

FIG. 8. Scatter plots of (u', v') at different times and meridional locations (ms^{-1}): at the initial linear stage, day $t = 20$ (left column), at some intermediate time, day $t = 39$, before the eddy tilt had flipped (middle column) and at day $t = 54$ after the eddy tilt had flipped (right column). This is shown for meridional locations of $y = b$ (upper row), $y = 0$ (middle row) and $y = -b$ (lower row). The red ellipse in each panel shows the corresponding calculated ellipse.

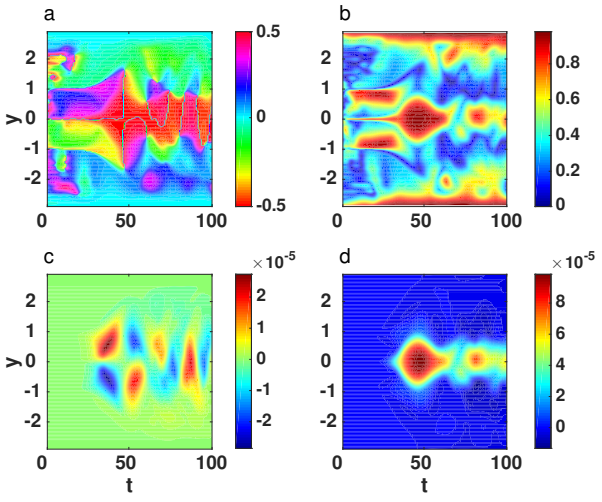

FIG. 9. Temporal evolution and meridional structure of (a) eddy ellipse tilt (normalized by π), (b) anisotropy, (c) $N = \overline{v'u'}$ ($\mathrm{m}^2\mathrm{s}^{-2}$) and (d) $M = \frac{1}{2}\left(\overline{v'^2} - \overline{u'^2}\right)$ ($\mathrm{m}^2\mathrm{s}^{-2}$). Note that the colorbar is cyclic in (a) Here $y = y/b$ is the nondimensional meridional coordinate.

This picture is confirmed by calculating the eddy variance ellipse at different times of the simulation. Fig. 8 shows scatter plots of u' and v' at the interfaces $y = \pm b, 0$ for three different times, as well as their corresponding ellipses (given by Eq. (12)). At day $t = 20$ (left column), the anisotropy is close to one near the interfaces, and the eddy ellipses are indeed very much elongated. In addition, the tilts are consistent with the linear instability picture, i.e. positive (negative) tilt in the cyclonic (anticyclonic) side of the jet. By day $t = 39$, anisotropy at the flanks $y = \pm b$ has become gradually smaller (hence the eddy ellipses appear more round), though they are still characterized by a tilt that implies barotropic instability. However, this changes at later times (day $t = 54$), when the ellipses at $y = \pm b$ are tilted oppositely, implying that the eddies are fluxing momentum up-gradient into the jet, with back-scatter of eddy energy to the mean flow. Note that at $y = 0$ (the center of the jet), we always find $\gamma = 1$ and $\theta = \pi/2$ (in fact, $\theta = \pi/2$ or 0 is required by symmetry), i.e., $N \cong 0$ and $M > 0$, the latter associated with $\overline{v'^2} \gg \overline{u'^2}$ such that the eddy variance ellipse is elongated in the meridional direction.

Fig. 9 shows the temporal development and meridional dependence of the zonally averaged eddy ellipse tilt and anisotropy, and of the Reynolds stresses M and N. Fig. 9a confirms that during the initial development of the system, in the time interval $t < 48$, the eddy tilt shows the signature of instability with positive tilts the in the cyclonic side of the jet and negative tilts the in the anticyclonic side of the jet. Gradually, the tilt (absolute value) in both sides of the jet approaches $\pi/2$, until at $t \approx 48$ all the eddies within the jet are characterized by $\theta = \pi/2$. The tilt then flips, consistent with the onset of stability and the momentum fluxes being directed up-gradient into the core of the jet. This holds until approximately day $t = 60$, after which a periodic behaviour with time can be identified.

The jet also broadens as a consequence of the instability, which not only acts to weaken the maximum jet velocity, but also increase the velocity at the flanks (see also Fig. 6a for the zonal mean velocity profiles at different times).

Fig. 9b shows the time evolution of the eddy anisotropy. During the initial time development there are three distinct regions where anisotropy is close to unity, at each of the interfaces $y = \pm b, 0$. During the transition period ($t \approx 48$), this picture changes drastically, with anisotropy being maximized in a broad meridional region around the jet center (the quasi-circular area of anisotropy close to unity around $t \approx 48$).

Fig. 9c shows the time development of N, which reveals the expected behaviour in the unstable period ($t < 48$) with N positive in the cyclonic side of the jet and negative in the anticyclonic side of the jet, and the opposite in the following stable period ($48 < t < 60$). As can be seen, the sign of the eddy ellipse tilt is controlled by the sign of the momentum flux N. The time evolution of M (Fig. 9d) is characterized by large positive values that are maximized around the jet core in the transition time $t \approx 48$, similar to the structure observed in the eddy anisotropy field. The

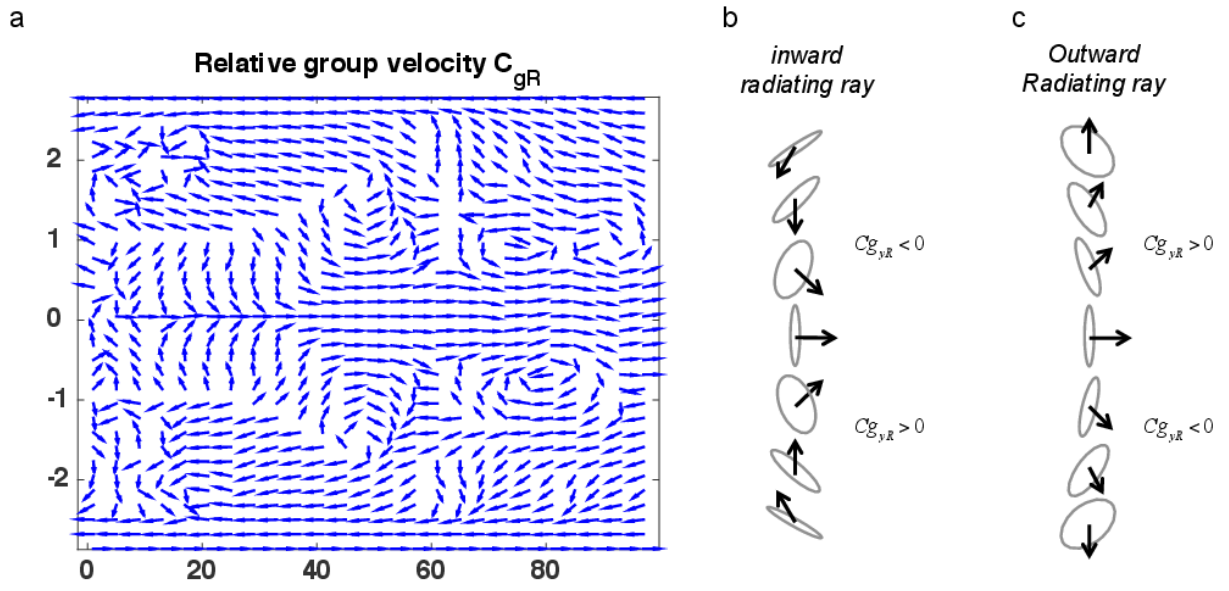

FIG. 10. (a) Direction of relative group velocity θc_{g_R}. Arrows show $(\cos\theta c_{g_R}, \sin\theta c_{g_R})$ and therefore denote only the direction of propagation. Here $y = y/b$ is the nondimensional meridional coordinate. (b) Schematic illustration of the zonally averaged eddy ellipse at different meridional locations, for the inward radiating ray, where eddy momentum fluxed are out of the jet and tend to decelerate it, and for the outward radiating ray (c), where the eddy momentum fluxes are into to jet and act to strengthen it.

large values of positive M together with $N \cong 0$ there, imply, as before, $\overline{v'^2} \gg \overline{u'^2}$.

d. Relative group velocity and relation to eddy ellipse tilt

A close relationship exists between the relative group velocity and the eddy ellipse tilt as given by (20) and sketched in Fig. 2. The direction of the relative group velocity from the simulation, estimated from the ratio N/M as in (19) is plotted in Fig. 10a.

During the unstable period ($t < 48$), the group velocity is directed inward, towards the jet core. In the initial moments of the instability ($t \approx 10$), the direction is almost independent of y and $c_{g_{R_y}}$ (the meridional component of y) is negative in the cyclonic side of the jet, consistent with the positive eddy ellipse tilt, and positive in the anticyclonic side of the jet, consistent with the negative eddy ellipse tilt. Hence, momentum is fluxed out of the jet. The direction of the relative group velocity at $t \approx 10$ is approximately $\theta c_{g_R} \approx \mp 0.65\pi$, giving $\theta \approx \pm 0.175\pi$ in the cyclonic and anticyclonic sides of the jet, respectively, which is close to the eddy ellipse tilt found in section (b) for the piecewise linear jet on an f plane. Shortly afterwards, however, the direction of relative group velocity is no longer independent of y; instead it increases in the cyclonic side and decreases in the anticyclonic side, with $\theta c_{g_R} \to 0$ at the jet core. This is consistent with the eddy ellipse turning towards $\theta = \pi/2$, i.e. meridional elongation.

A schematic illustration of the inward radiating ray is shown in Fig. 10b, which outlines the averaged eddy ellipse as a function of the meridional location, together with the direction of the relative group velocity, during the unstable regime. Note that although the direction of the relative group velocity changes significantly, it always has a negative meridional component and positive ellipse tilt on the cyclonic side of the jet and a positive meridional component and negative ellipse tilt on the anticyclonic side of the jet, hence fluxing momentum out of the jet.

As the jet transitions to the stable regime as the absolute vorticity gradient ceases to change sign at $t \approx 48$, all the rays become zonal ($\theta c_{g_R} = 0$, $\theta = \pi/2$) and the eddy ellipse is meridionaly elongated. Immediately thereafter, we enter the stable regime with outward radiating rays. The sign of the meridional component of the relative group velocity changes to positive on the cyclonic side of the jet and negative on the anticyclonic side of the jet. The outward radiating ray is illustrated in Fig. 10c. Going away from the jet core, the ray becomes refracted such that it becomes more meridional, consistent with negative ellipse tilt on the cyclonic side of the jet and positive ellipse tilt on the anticyclonic side of the jet, hence fluxing momentum up-gradient into the jet.

e. Comparison with Waterman and Hoskins (2013)

It is interesting to make, at this point, a comparison between the results obtained here and those obtained by Waterman and Hoskins (2013) for the case of a zonally evolving jet in statistically steady state. In Waterman and Hoskins (2013) an unstable jet is forced at the boundary of the domain, and the geometric properties of the horizontal velocity correlation tensor are defined via time mean averaging, rather than zonal averaging. The analysis shows a similar picture to that described here: eddies tilting against the shear in the upstream unstable region, and an eddy tilt consistent with wave radiation observed in the downstream stable region. The broad structure of M, N, K and the corresponding eddy ellipses described in Waterman and Hoskins (2013) are remarkably similar to those found here but, importantly, in Waterman and Hoskins (2013) the structure varies spatially along the flow direction, whereas here the structure varies temporally through the flow evolution.

There are, however, some interesting differences. First, in Waterman and Hoskins (2013), the location where the eddy kinetic energy maximizes occurs downstream of the location where the potential vorticity gradient ceases to change sign as a consequence of mean flow advection, whereas in our case they occur simultaneously in time. At the point of maximum eddy kinetic energy, Waterman and Hoskins also find a "bullet of M", implying meridional elongation of the eddies there.

Downstream of eddy kinetic energy maximum, Waterman and Hoskins find that forcing solely from M is responsible for strengthening and extending the jet, eventually forcing their time-mean recirculation gyres. In our case, however, since we consider a zonally symmetric jet, the zonal mean vorticity forcing from M vanishes, so all the mean flow forcing arises from N. Moreover, no recirculation gyres can develop in our configuration, and the eddy forcing is instead responsible for the acceleration of the jet.

4. Ray tracing

For a barotropic jet on a β-plane during the unstable regime, the eddy ellipse tilt is no longer constant within the layers (see Fig. 12a), but rather it increases towards the jet core. This effect is purely due to the continuous potential vorticity gradient, and is intrinsically related to the wave propagation. If we attempt to solve the propagation of perturbations away from the interfaces, i.e. inside each side of the jet, then the dispersion relation is mainly influenced by the β term. In other words, we can ignore the $-\partial^2\bar{u}/\partial y^2$ term in the mean potential vorticity gradient (which in the piecewise linear jet model is exactly zero, except at the three fronts).

We now make use of ray tracing theory to study the propagation of waves within the shear layers, under the influence of the β effect and constant shear. The analytic solution obtained from the ray equations not only agrees well with the fully nonlinear simulation, but also helps us understand the meridional structure of the eddy ellipse tilt. Let us first briefly review ray tracing theory and the basic governing equations.

a. Theoretical background

The wave activity propagates at a velocity equal to the group velocity. In a homogeneous medium, a ray (which is the path parallel to the group velocity at every point) will propagate in a straight line. In an inhomogeneous medium, however, refraction can occur. Ray tracing theory (Whitham 1974; Lighthill 1977, also see Buhler 2009 and Salmon (1998) for overviews) gives the leading order asymptotic description of a slowly varying wavetrain in a medium that varies slowly compared to the scale of the waves (through the WKBJ approximation, see Hoskins and Karoly 1981; Hoskins and Ambrizzi 1993).

For such conditions, the streamfunction can be represented locally by a plane wave,

$$\psi(x,y,t) \sim \hat{\psi} e^{i\phi(x,y,t)} \tag{43}$$

with

$$\phi \approx kx + ly - \omega t, \tag{44}$$

where

$$\omega(x,y,t) = -\frac{\partial \phi}{\partial t}, \quad k(x,y,t) = \frac{\partial \phi}{\partial x}, \quad l(x,y,t) = \frac{\partial \phi}{\partial y} \tag{45}$$

are slowly varying. Note that here a distinction is made between the local value of the angular frequency, $\omega(x,y,t)$, and the dispersion relation, $\Omega(k,l,x,y,t)$, with $\omega(x,y,t) = \Omega(k(x,y,t),l(x,y,t),x,y,t)$. Cross-differentiation then leads to the ray equations

$$\frac{dk}{dt} = -\frac{\partial \Omega}{\partial x}, \qquad \frac{dl}{dt} = -\frac{\partial \Omega}{\partial y}, \tag{46}$$

along rays defined by

$$\frac{dx}{dt} = c_{gx} = \frac{\partial \Omega}{\partial k}, \qquad \frac{dy}{dt} = c_{gy} = \frac{\partial \Omega}{\partial l}, \tag{47}$$

where

$$\frac{d}{dt} = \frac{\partial}{\partial t} + \mathbf{c}_g \cdot \nabla. \tag{48}$$

These are equivalent to Hamilton's equations in classical mechanics. In the absence of explicit time dependence in $\Omega(k,l,x,y,t)$, the analogue of the Hamiltonian, is conserved along the ray path.

b. Analytical ray tracing solution

In the case considered here, away from the interfaces we can approximate the solutions as plane waves on a β plane, whose dispersion relation is given by

$$\Omega = \bar{u}k - \frac{\beta k}{k^2+l^2}, \tag{49}$$

where $\bar{u} = \Lambda(b-y)$ on the cyclonic ($y>0$) side of the jet, and $\bar{u} = \Lambda(b+y)$ on the anticyclonic ($y<0$) side of the jet. It follows that

$$\frac{dk}{dt} = 0, \qquad \frac{dl}{dt} = -k\frac{\partial \bar{u}}{\partial y} = \pm k\Lambda; \tag{50}$$

$$\frac{dx}{dt} = \bar{u} + \frac{\beta(k^2-l^2)}{(k^2+l^2)^2}, \quad \frac{dy}{dt} = \frac{2\beta kl}{(k^2+l^2)^2}, \tag{51}$$

where $\pm$ refers to $y>0$ and $y<0$ respectively. Hence, we find that

$$k = k_0, \quad l = l_0 \mp k\Lambda t \tag{52}$$

where k_0 and l_0 are the initial zonal and meridional wavenumbers.

The set of ray equations (50) and (51) may be solved analytically (see Appendix C for a full derivation). The analytic solution for the eddy ellipse tilt as a function of the meridional location gives

$$\theta(y) = \pm\frac{1}{2}\cos^{-1}\left(\cos 2\theta_0 \mp \frac{2\Lambda k_0^2}{\beta}(y-y_0)\right). \tag{53}$$

which allows us to investigate how the ray solution depends on the parameters of the problem, namely β, k and the shear Λ. Note that the solution, conveniently, does not depend on k_0, l_0, but rather on the initial tilt $\theta(y_0) = \theta_0$, which can be calculated directly from the Reynolds stresses (11).

For example, for an outward radiating ray on the cyclonic side of the jet, originating at the jet center, we would have $y_0 = 0$, $\theta_0 = \pi/2$ and $\partial\bar{u}/\partial y = -\Lambda$, giving

$$\theta(y) = \frac{1}{2}\cos^{-1}\left(\frac{2\Lambda k^2}{\beta}y - 1\right). \tag{54}$$

Note that the solution is only valid for $0 < y \le \beta/\Lambda k^2$. If $\Lambda = 0$, we find that $\theta(y) = \theta_0 = \pi/2$, i.e. the tilt is constant (indeed, a plane wave propagating on a β plane without background flow is characterized by constant k_0, l_0, constant group velocities and therefore straight ray lines). If $\beta = 0$, the solution is not well defined since the ray does not propagate in the first place (the relative group velocities are zero). For nonzero β and Λ, going away from the jet core towards the flank at $y = b$, the tilt becomes gradually smaller, approaching $\theta \to 0$ for $y \to \beta/\Lambda k^2$. This is consistent with the results of the previous section for the outward radiating ray (compare with Fig. 10). The analytic solution also implies that for larger wavenumber, larger shear, or smaller β, the tilt decreases faster when moving away from the jet core, which means that the ray is refracted more.

Since it is the shear which is responsible for the refraction of the rays (through changing the meridional wavenumber $l = l_0 \mp k\Lambda$t), it is clear that a larger shear will cause larger refraction. The wavenumber dependence is also clear, since larger wavenumbers corresponds to smaller waves, which are more easily influenced by the background shear. Finally, β has a competing effect with the shear. To better illustrate this, we rewrite the first term inside the $\cos^{-1}$ in (54) in terms of the nondimensional β term $\beta^* = \beta b/\Lambda$, which measures the importance of the planetary vorticity gradient relative to the mean shear, the normalized nondimensional wave number $\tilde{k} = 2kb$, and the normalized nondimensional meridional coordinate, $Y = y/2b$, where $2b$ is the width of the jet. This gives $(2\Lambda k^2/\beta)y = (\tilde{k}^2/\beta^\star)Y$. Hence, if $\beta^\star \ll 1$ (which means that βb is small relative to the shear), the coefficient of Y is large so the tilt changes rapidly when moving away from the core, and correspondingly, the ray is significantly refracted. If, on the other hand, $\beta^\star \gg 1$ (that is, the shear is small relative to βb), then the tilt and hence ray path does not vary significantly.

c. Comparison with numerical results

The validity of the analytic solution is now verified by comparing it with numerical ray tracing results. We solve the ray equations (50) and (51) using a forward Euler time stepping. In Fig. 11 we plot the results of the ray tracing for different choices of initial zonal wavenumber, k_0. For the inward radiating ray, we initiate the ray just slightly below and above the upper and lower interfaces $y = b$, $-b$ respectively. We specify k_0 and find l_0 such that the eddy ellipse tilt (assuming plane wave solutions) is equal to the value diagnosed at that point from the simulation. That is, given k_0 and y_0, we find l_0 such that

$$\tan 2\theta(y_0) = \frac{2k_0 l_0}{k_0^2 - l_0^2}, \tag{55}$$

which gives two possible solutions for l_0. We choose the sign such that the ray is directed towards the jet, i.e., $l_0 < 0$ in the cyclonic side of the jet and $l_0 > 0$ in the anticyclonic side of the jet. The possible values for k_0 can be evaluated using $k^\star \approx (\overline{v'v'}/\overline{\psi'\psi'})^{1/2}$. This gives a typical value of $k^\star \approx 3.6\times10^{-6}\,\mathrm{m}^{-1}$ or, in normalized units, $2k^\star b \cong 3.1$ (where $b = 430$km is the width of the shear layer in each side of the jet). This is not very far from the theoretical value for the most unstable mode ($2k_{max}b \cong 2.452$), found for the case of a piecewise linear jet without β.

In Fig. 11a we plot the relative group velocity from the ray tracing, for rays with varying zonal wavenumbers

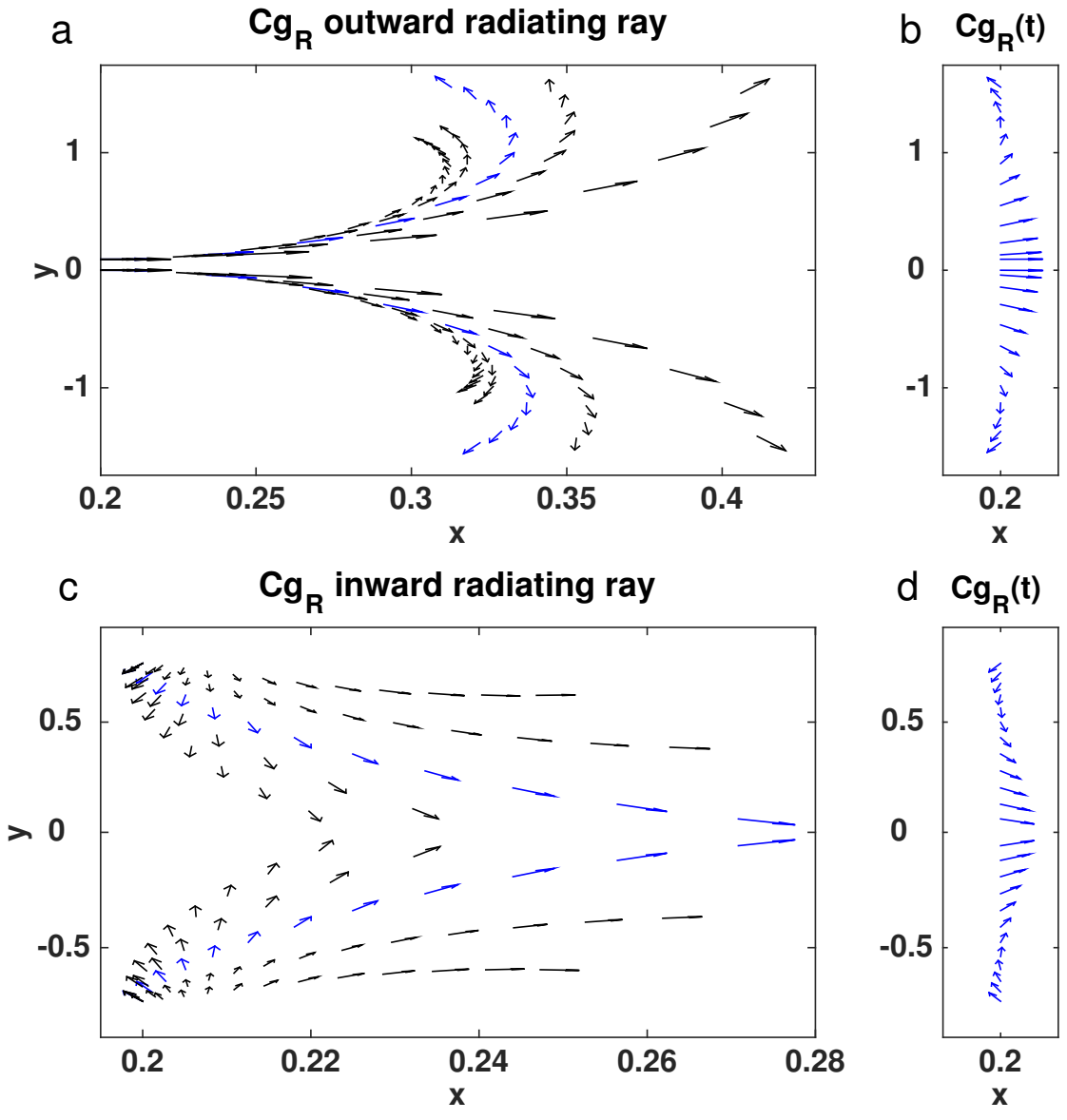

FIG. 11. (a) Direction of relative group velocity from ray tracing results for the inward radiating ray, for varying zonal wavenumbers: $k_0 = 0.25k^\star, 0.3k^\star, 0.4k^\star, 0.5k^\star, 0.9k^\star$. The leftmost ray corresponds to the smallest wavenumber. The track for $k_0 = 0.4k^\star$ is highlighted in blue for reference. (b) The highlighted ray with $k_0 = 0.4k^\star$ as a function of time, in the same zonal location. (c) Outward radiating ray, for varying zonal wavenumbers: $k_0 = 0.2k^\star, 0.26k^\star, 0.3k^\star, 0.34k^\star, 0.38k^\star$. The leftmost ray corresponds to the largest wavenumber. The track for $k_0 = 0.3k^\star$ is highlighted in blue for reference. (d) The highlighted ray with $k_0 = 0.3k^\star$ as a function of time, in the same zonal location. Note that in all panels arrows are unitless and show only the direction of relative group velocity. Here $y = y/b$ is the nondimensional meridional coordinate.

$k_0 = 0.25k^\star$, $0.3k^\star$, $0.4k^\star$, $0.5k^\star$ and $0.9k^\star$, where the leftmost ray corresponds to the smallest wavenumber. The track for $k_0 = 0.4k^\star$ is highlighted in blue for reference. In all cases, the initially southwestward pointing ray ends up pointing eastward pointing, i.e., θc_{gR} tends towards zero as the rays approach the core of the jet, just as in the results from the numerical simulation analysed in section 3d. The meridional component of the relative group velocity, however, remains negative in the cyclonic side of the jet, implying a positive eddy ellipse tilt, and vice-versa in the anticyclonic side of the jet, i.e. the momentum fluxes point out of the jet. Since the rays are plotted as a function of the

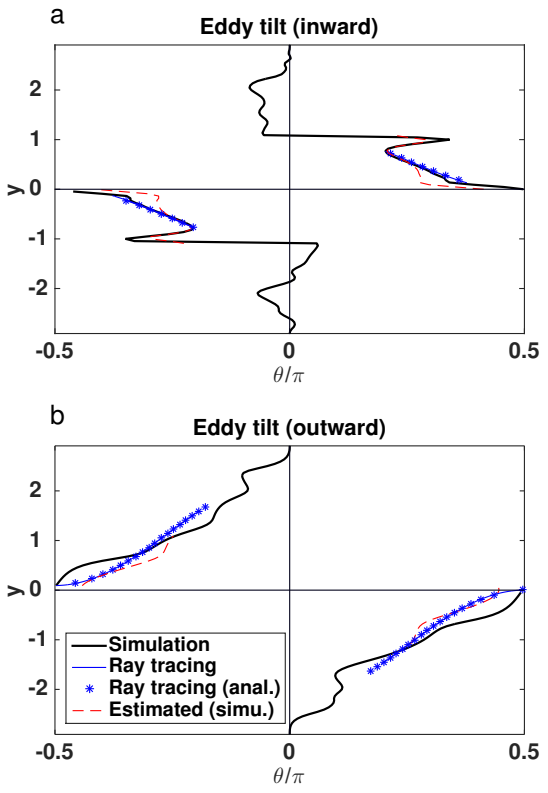

FIG. 12. Eddy ellipse tilt (normalized by π), for (a) inward radiating ray (day $t = 25$) and (b) outward radiating ray (day $t = 55$). Compared are actual tilt (red), estimated value (dashes black), ray tracing results from numerical (blue) and analytic (green stars) solutions. See text for explanation. Here $y = y/b$ is the nondimensional meridional coordinate.

zonal location x rather than time, in Fig. 11b we also plot the highlighted ray with $k_0 = 0.4k^\star$ as a function of time, in the same zonal location (this is equivalent to plotting the zonal average of the left figure). Note the remarkable similarity with Fig. 10a for the inward radiating ray during the unstable regime, as well as the schematic illustration of it in Fig. 10b.

For the outward radiating ray, we initiate the ray very close to the jet core ($y = 0$) and hence we set $l_0 = 0$ which means that $\theta = \pi/2$ and $\theta c_{gR} = 0$. We choose the sign of the ray tracing solution such that the ray is directed outwards from the jet, i.e., l positive on the cyclonic side of the jet and negative on the anticyclonic side of the jet. In Fig. 11c we plot the relative group velocity from the ray tracing for the outward propagating rays for zonal wavenumbers $k_0 = 0.2k^\star$, $0.26k^\star$, $0.3k^\star$, $0.34k^\star$ and $0.38k^\star$ where the leftmost ray corresponds to the largest wavenumber. This is consistent with our earlier inspection of the analytic solution for the outward radiating ray, where we found that larger wavenumbers will tend to be refracted more. The track for $k_0 = 0.3k^\star$ is highlighted in blue for reference. In all cases, θc_{gR} increases in the cyclonic side and decreases in the anticyclonic side towards the jets flanks, similar to that observed in the simulation for the stable outward radiating regime. The meridional component of the relative group velocity remains positive, which implies a negative eddy ellipse tilt in the cyclonic side of the jet and vice-versa on the anticyclonic side of the jet, i.e., momentum fluxes into the jet. In Fig. 11d we plot the highlighted ray with $k_0 = 0.3k^\star$ as a function of time in the same zonal location. This is again remarkably similar to Fig. 10 for the stable, outward radiating regime, and to the schematic illustration of the outward radiating ray in Fig. 10c.

Finally, in Fig. 12a, b we compare the eddy ellipse tilt from the simulation and the ray tracing, for the inward (day $t = 25$) and outward (day $t = 55$) radiating rays, respectively. We use both the actual value for the tilt (black thick line), calculated from the simulation using the Reynolds stresses (11), as well as the estimated value (dashed thin red line) for a plane wave solution (14) using the estimated meridional and zonal wavenumbers $l^\star \approx (\overline{u'u'}/\overline{\psi'\psi'})^{1/2}$, $k^\star \approx (\overline{v'v'}/\overline{\psi'\psi'})^{1/2}$, respectively, evaluated locally at every y. For the ray tracing solution, we choose $k_0 = 0.4k^\star$ for the inward radiating ray and $k_0 = 0.3k^\star$ for the outward radiating ray (the blue rays in Figs. 11a and 11c, respectively). As a check for our analytic solution for the ray tracing equations, we plot both the numerical (blue thin line) and the analytic solution (blue stars) for the eddy ellipse tilt, and these indeed coincide. As can be seen, the ray tracing agrees well with the simulation (albeit with the particular choices for the zonal wavenumbers as described above), and captures correctly the overall dependence of the tilt with y. The estimated tilt value using the estimated local wavenumbers also gives good agreement with the actual tilt value, which means that the plane wave assumption works reasonably well.

5. Summary and discussion

In this manuscript, we have revisited the role of eddy Reynolds stresses in accelerating and decelerating barotropic ocean jets. In particular, we have analysed the eddy Reynolds stresses by exploring the geometric properties of the eddy stress tensor. This eddy stress tensor can be described in terms of an eddy variance ellipse, the geometry of which characterizes the mean eddy shape and orientation, the direction of eddy activity propagation, and the eddy forcing of the mean flow.

Idealized linear shear and jet profiles have been analysed and the theoretical results compared against fully nonlinear simulations. For flows with zero planetary vorticity gradient, analytic solutions have been obtained and

provide a direct relationship between the geometric eddy tilt and the phase difference of a normal mode solution. This allows a straightforward interpretation in terms of classical stability theory: the initially unstable jet gives rise to eddies that are tilted against the shear and extract energy from the mean flow. Once the jet stabilizes, eddies become tilted with the shear and return their energy to the mean flow. For a non-zero planetary vorticity gradient, ray-tracing theory has been used to investigate eddy propagation within the jet. An analytic solution for the eddy tilt has been obtained for a linear plane Rossby wave on a constant background shear, the results of which agree broadly with the eddy tilts diagnosed from a fully nonlinear simulation.

We propose that the geometric framework explored in this manuscript could be used as a diagnostic tool to understand the role of Reynolds stresses in maintaining and decelerating inertial jets in ocean models and observations. For example, similar ideas have already been applied to separated western boundary currents such as the Gulf Stream and Kuroshio (Waterman and Hoskins 2013) and are currently being applied to the Southern Ocean to elucidate how the zonal jets embedded within the Antarctic Circumpolar Current vary with longitude (Klocker et al., manuscript in preparation). For such problems, it would be interesting to apply the same ray tracing methods employed to see if they can provide similar insights for flows that vary in all three spatial dimensions and time. Recent theoretical developments (e.g., Waterman and Lilly 2015) provide further avenues for exploration.

Moreover, we propose that a simple version of the approach taken here might be employed to develop a simple parameterization of eddy Reynolds stresses for ocean general circulation models that are able to (at least partially) resolve inertial jets. While it is surely impractical to contemplate solving ray equations in such models, one could imagine assuming that some of the eddy energy generated through baroclinic instability is back-scattered to the mean flow by up-gradient momentum transfer, as found in some of the idealized jet profiles in this manuscript, and proposed, for example, by Marshall and Adcroft (2010) and Jansen and Held (2014).

Exploiting the fact that the component of the eddy stress tensor involving the eddy Reynolds stresses is bounded by the eddy kinetic energy, assuming the momentum fluxes are directed up-gradient (say at $\mp\pi/2$ relative to the mean flow), and prescribing a typical value for the eddy anisotropy, it should be possible to develop a simple parameterization that is both energetically consistent and rooted in the underlying geometry of the eddy dynamics. Even at the simplest level, there remain many questions to be addressed, for example, should such a parameterization be applied to the depth-integrated flow? Furthermore it will be necessary to model the formation, propagation and dissipation of eddy kinetic energy, as discussed by Eden and Greatbatch (2008); Marshall and Adcroft (2010); Jansen et al. (2015). Despite these challenges, we believe this approach holds some promise and is worth exploring further.

APPENDIX A

Generalization of the relations for M and N between any pair of vorticity waves

The two isolated δ-function vorticity waves can be generalized to the case where the vorticity field is continuous. Consider a zonal Fourier component of the vorticity anomaly,

$$q' = \widetilde{q}_k(x,y,t)e^{ikx} = \widetilde{Q}_k(y,t)e^{i(kx+\varepsilon_k(y,t))}, \tag{A1}$$

inducing a streamfunction anomaly of the form

$$\psi' = \int \widetilde{q}_k(x,y,t)G(y,y')dy'e^{ikx}, \tag{A2}$$

where the Green's function is given by

$$G(y,y') = -\frac{1}{2k}e^{-k|y-y'|}. \tag{A3}$$

After some algebra, we obtain

$$M = \iint \frac{\widetilde{Q}_k(y',t)\widetilde{Q}_k(y'',t)}{4}e^{-k(y'-y'')} \cos(\varepsilon_k(y'',t)-\varepsilon_k(y',t))dy'dy'' \tag{A4a}$$

$$N = -\iint \frac{\widetilde{Q}_k(y',t)\widetilde{Q}_k(y'',t)}{4}e^{-k(y'-y'')} \sin(\varepsilon_k(y'',t)-\varepsilon_k(y',t))dy'dy'' \tag{A4b}$$

Hence the values of M and N at some location y can be regarded as resulting from the continuum of infinite number of pairs of vorticity waves sandwiching y from below (y' contributions in the integral) and from above (y'' contributions in the integral).

APPENDIX B

Numerical model description

For this study, we use PEQUOD ("Parallel Quasi-Geostrophic Model"), a finite differences code for solving quasi-geostrophic equations in a rectangular domain, configured in a one layer barotropic configuration. The numerical method implemented in PEQUOD and used here incorporates the Compact Accurately Boundary Adjusting high-Resolution Technique (CABARET) for advection of relative potential vorticity, combined with integration of the advection of planetary vorticity. The CABARET scheme is a potential vorticity-conserving,

second-order (in space and time) accurate method, incorporating a non-linear flux limiter. Further details can be found in Karabasov and Goloviznin (2007) and Karabasov et al. (2009). The potential vorticity inversion is performed using a fast Poisson solver using a customized version of FFTPACK.

The simulations are conducted in a rectangular domain $-L \le x \le L$, $-0.5L \le y \le 0.5L$ where $L = 2500$km, with a no-slip boundary condition applied to the perturbation from the background profile, at all lateral boundaries. The model is integrated using a grid of $n_x = 256$ and $n_y = 129$ nodes in the zonal and meridional directions, respectively, corresponding to 19km resolution and with a time step size of 1800s. The model is then run for 100 days. The eddies are defined as deviations from the zonal mean, and the corresponding eddy quantities such as eddy kinetic energy, Reynolds stresses and the eddy variance ellipse parameters calculated accordingly.

We initialize the flow with the zonally symmetric jet U_0 which is barotropically unstable, and perturb it with a small random noise. The numerical model essentially solves

$$\frac{Dq}{Dt} = \nu\nabla^2 q - r(q - q_{eq}) \tag{B1}$$

where $q = \nabla^2\psi + \beta y$ is the absolute vorticity, $\nu = 100\,\mathrm{m^2\,s^{-1}}$ is a Laplacian viscosity coefficient parameter, and $r = 1.5\times10^{-8}\,\mathrm{s^{-1}}$ is the relaxation time scale towards the background equilibrium flow $q_{eq} = q_0$. We set $U_{0max} = 0.04\,\mathrm{m\,s^{-1}}$, and the width of our jet is $2b = 860$km. This corresponds to a linear growth rate of approximately $\sim 0.24\Lambda = 2.2\times10^{-8}\,\mathrm{s^{-1}}$, which is the linear growth rate of the most unstable mode as shown in Heifetz et al. (1999), where Λ is the shear and equals $\Lambda = U_{0max}/b \cong 9.3\times10^{-8}\,\mathrm{s^{-1}}$ in our case. For the case where the planetary vorticity gradient is nonzero, we use $\beta = 10^{-13}\,\mathrm{m^{-1}\,s^{-1}}$ which corresponds to a non dimensional β (which measures the relative importance of the planetary vorticity gradient relative to the mean shear) of $\beta^* = \beta b/\Lambda \cong 0.46$. For comparison, the non dimensional β of a typical ocean jet can be evaluated by $\beta^* = \beta W^2/U$ where W is the width of the jet, and U is the typical jet speed. In midlatitudes $\beta \sim 2\times10^{-11}\,\mathrm{m^{-1}\,s^{-1}}$, and for a typical ocean jet $U \sim 2\,\mathrm{m\,s^{-1}}$ and $W \sim 100$km, leading to $\beta^* \sim 0.1$. Our effective β is a bit larger, which means that our jet is possibly influenced more by the β term, but is of similar order.

APPENDIX C

Analytic solution for the ray tracing equations

Solving the ray equations (50) and (51) gives

$$k(t) = k_0, \quad l(t) = l_0 \pm k_0\Lambda t, \tag{C1}$$

where k_0, l_0 are the initial wavenumbers.

Next we can use

$$\frac{dy}{dt} = \frac{2\beta kl}{(k^2+l^2)^2} = \frac{2\beta}{k_0^2}\frac{\left(\frac{l_0}{k_0}\pm\Lambda t\right)}{\left[1+\left(\frac{l_0}{k_0}\pm\Lambda t\right)^2\right]^2}, \tag{C2}$$

giving

$$y(t) = y_c \mp \frac{\beta}{\Lambda k_0^2}\frac{1}{\left[1+\left(\frac{l_0}{k_0}\pm\Lambda t\right)^2\right]} \tag{C3}$$

where y_c is an integration constant. Similarly, using

$$\frac{dx}{dt} = \frac{\beta(k^2-l^2)}{(k^2+l^2)^2}, \tag{C4}$$

we find

$$x(t) = x_c \mp \frac{\beta}{\Lambda k_0^2}\frac{\left(\frac{l_0}{k_0}\pm\Lambda t\right)}{\left[1+\left(\frac{l_0}{k_0}\pm\Lambda t\right)^2\right]}. \tag{C5}$$

These are the analytic solutions describing the ray path, following the relative group velocity.

Now substituting the above expressions in (15), we have

$$\tan\theta = \frac{l_0}{k_0} \pm \Lambda t \tag{C6}$$

and, substituting into (C3),

$$y(t) - y_c = \mp\frac{\beta}{\Lambda k_0^2}\cos^2\theta = \mp\frac{\beta}{2\Lambda k_0^2}(\cos 2\theta + 1). \tag{C7}$$

At $t = 0$, we find:

$$y_0 - y_c = \mp\frac{\beta}{2\Lambda k_0^2}(\cos 2\theta_0 + 1). \tag{C8}$$

Hence

$$y(\theta) = y_0 \mp \frac{\beta}{2\Lambda k_0^2}(\cos 2\theta - \cos 2\theta_0). \tag{C9}$$

Finally, solving for θ gives

$$\theta(y) = \pm\frac{1}{2}\cos^{-1}\left(\cos 2\theta_0 \mp \frac{2\Lambda k_0^2}{\beta}(y - y_0)\right), \tag{C10}$$

which is (53), where $\mp 2\Lambda k^2/\beta$ is negative in the cyclonic side of the jet ($y > 0$) and positive in the anticyclonic side of the jet ($y < 0$). The two possible $\pm$ solutions corresponds to the two possible solutions for l.

Acknowledgments. The authors would like to gratefully acknowledge useful discussions Laure Zanna. JRM and DPM acknowledge the partial support of the Natural Environment Research Council, NE/L005166/1. The numerical code used in this article was developed from an original code provided by Pavel S. Berloff.

References

Bretherton, F. P., 1966a: Baroclinic instability, the short wave cutoff in terms of potential vorticity. *Q. J. R. Meteorol. Soc.*, **92**, 335–345.

Bretherton, F. P., 1966b: Critical layer instability in baroclinic flows. *Q. J. Roy. Meteorol. Soc.*, **92**, 325–334.

Buhler, O., 2009: *Waves and Mean Flows*. Cambridge University Press, 341 pp.

Cronin, M., 1996: Eddy-mean flow interaction in the gulf stream at 68°W. Part II: Eddy forcing on the time-mean flow. *J. Phys. Oceanogr.*, **26**, 2132–2151.

Danabasoglu, G., J. C. McWilliams, and P. R. Gent, 1994: The role of mesoscale tracer transport in the global ocean circulation. *Science*, **264**, 1123–1126.

Eden, C., 2010: Parameterising meso-scale eddy momentum fluxes based on potential vorticity mixing and a gauge term. *Ocean Modell.*, **32 (1-2)**, 58–71.

Eden, C., and R. J. Greatbatch, 2008: Towards a mesoscale eddy closure. *Ocean Modell.*, **20**, 223–239.

Fox Kemper, B., R. Lumpkin, and F. Bryan, 2013: Lateral transport in the ocean. *Ocean Circulation and Climate (Second edition)*, G. Siedler, J. Church, J. Gould, and S. Griffies, Eds., 185–209.

Gent, P., and J. McWilliams, 1996: Eliassen-palm fluxes and the momentum equation in non-eddy-resolving ocean circulation models. *J. Phys. Oceanogr.*, **26**, 2539–2546.

Gent, P. R., and J. C. McWilliams, 1990: Isopycnal mixing in ocean circulation models. *J. Phys. Oceanogr.*, **20**, 150–155.

Gent, P. R., J. Willebrand, T. J. McDougall, and J. C. McWilliams, 1995: Parameterizing eddy-induced tracer transports in ocean circulation models. *J. Phys. Oceanogr.*, **25**, 463–474.

Greatbatch, R. J., 1998: Exploring the relationship between eddy-induced transport velocity, vertical momentum transfer, and the isopycnal flux of potential vorticity. *J. Phys. Oceanogr.*, **28**, 422–432.

Heifetz, E., C. H. Bishop, B. J. Hoskins, and P. Alpert, 1999: Counter-propagating Rossby waves in barotropic Rayleigh model of shear instability. *Q. J. R. Meteorol. Soc.*, **125**, 2835–2853.

Hoskins, B. J., and T. Ambrizzi, 1993: Rossby wave propagation on a realistic longitudinally varying flow. *J. Atmos. Sci.*, **50**, 1661–1671.

Hoskins, B. J., I. N. James, and G. H. White, 1983: The shape, propagation and mean-flow interaction of large-scale weather systems. *J. Atmos. Sci.*, **40**, 1595–1612.

Hoskins, B. J., and D. J. Karoly, 1981: The steady linear response of a spherical atmosphere to thermal and orographic forcing. *J. Atmos. Sci.*, **38**, 1179–1196.

Jansen, M., A. Adcroft, R. Hallberg, and I. Held, 2015: Parameterization of eddy fluxes based on a mesoscale energy budget. *Ocean Modell.*, doi:10.1016/j.ocemod.2015.05.007.

Jansen, M., and I. Held, 2014: Parameterizing subgrid-scale eddy effects using energetically consistent backscatter. *Ocean Modell.*, **80**, 36–48.

Johnson, G. C., and H. L. Bryden, 1989: On the size of the Antarctic Circumpolar Current. *Deep Sea Res.*, **36**, 39–53.

Karabasov, A., P. Berloff, and V. Goloviznin, 2009: CABARET in the ocean gyre. *Ocean Modeling*, **30**, 155–168.

Karabasov, A., and V. Goloviznin, 2007: A new efficient high-resolution method for non-linear problems in fluid mechanics. *New Trends in Fluid Mechanics Research, Springer*, **1**, 269–272.

Lee, M.-M., and H. Leach, 1996: Eliassen-Palm flux and eddy potential vorticity flux for a nonquasigeostrophic time-mean flow. *J. Phys. Oceanogr.*, **26 (7)**, 1304–1319.

Lighthill, J., 1977: *Waves in Fluids*. Cambridge University Press, 504 pp.

Maddison, J. R., and D. P. Marshall, 2013: The Eliassen-Palm flux tensor. *Journal of Fluid Mechanics*, **729**, 69–102.

Marshall, D. P., and A. J. Adcroft, 2010: Parameterization of ocean eddies: Potential vorticity mixing, energetics and Arnold's first stability theorem. *Ocean Modell.*, **32**, 188–204.

Marshall, D. P., J. R. Maddison, and P. S. Berloff, 2012: A framework for parameterizing eddy potential vorticity fluxes. *J. Phys. Oceanogr.*, **42 (4)**, 539–557.

Morrow, R., R. Coleman, J. Church, and D. Chelton, 1994: Surface eddy momentum flux and velocity variances in the Southern Ocean from Geosat altimetry. *J. Phys. Oceanogr.*, **24**, 2050–2071.

Pedlosky, J., 1979: *Geophysical Fluid Dynamics*. Springer US, New York, NY.

Plumb, R., 1986: Three-dimensional propagation of transient quasi-geostrophic eddies and its relationship with the eddy forcing of the time-mean flow. *J. Atmos. Sci.*, **43**, 1657–1678.

Preisendorfer, R., 1988: *Principal Component Analysis in Meteorology and Oceanography*. Elsevier.

Salmon, R., 1998: *Lectures on geophysical fluid dynamics*. Oxford University Press.

Scott, R., B. Arbic, C. Holland, A. Sen, and B. Qiu, 2008: Zonal versus meridional velocity variance in satellite observations and realistic and idealized ocean circulation models. *Ocean Model.*, **23**, 102–112.

Taylor, G. I., 1915: Eddy motion in the atmosphere. *Phil. Trans. Roy. Soc. A*, **215**, 1–26.

Waterman, S., N. G. Hogg, and S. R. Jayne, 2011: Eddy-mean flow interaction in the Kuroshio Extension region. *J. Phys. Oceanogr.*, **41**, 1182–1208.

Waterman, S., and B. J. Hoskins, 2013: Eddy shape, orientation, propagation, and mean flow feedback in western boundary current jets. *J. Phys. Oceanogr.*, **43**, 1666–1690.

Waterman, S., and S. Jayne, 2012: Eddy-driven recirculations from a localized, transient forcing. *J. Phys. Oceanogr.*, **42**, 430–447.

Waterman, S., and S. R. Jayne, 2011: Eddy-mean flow interactions in the along-stream development of a western boundary current jet: An idealized model study. *J. Phys. Oceanogr.*, **41**, 682–707.

Waterman, S., and J. M. Lilly, 2015: Geometric decomposition of eddy feedbacks in barotropic systems. *J. Phys. Oceanogr.*, **45**, 1009–1024.

Whitham, G., 1974: *Linear and Nonlinear Waves*. New York: Wiley-Interscience.

Young, W. R., 2012: An exact thickness-weighted average formulation of the Boussinesq equations. *J. Phys. Oceanogr.*, **42**, 692–707.